Favored CH-π interaction between enzymatically modified high amylose starch and resveratrol improves digestion resistance

Zhipeng Qiu[a], RuiLi[a], Jin Chen[a*], Ling Chen[a**], Fengwei Xie[b]

[a]School of Food Science and Engineering, Guangdong Province Key Laboratory for Green Processing of Natural Products and Product Safety, Engineering Research Center of Starch and Vegetable Protein Processing Ministry of Education, South China University of Technology, Guangzhou 510640, China

[b]School of Engineering, Newcastle University, Newcastle Upon Tyne, NE1 7RU, United Kingdom

* Corresponding author: bravojinchen@scut.edu.cn (Jin Chen);

** Corresponding author: felchen@scut.edu.cn; (Ling Chen)

Abstract

Starch-stilbene polyphenol complexes, a novel form of resistant starch (RS), have received considerable attention due to their potential health benefits. To enhance the functionality of this type of complex, we examined the interactions between resveratrol (RA) and high-amylose starch with different molecular weights, achieved through enzymatic modification followed by high-pressure homogenization (HPH). We examined how these interactions affect the digestibility and ordered structures of the complexes. Our findings reveal that, notwithstanding the inhibition of double helix and B-type crystalline structure formation, RA-starch complexation markedly boosted single helix content, V-type crystalline structure formation, and aggregate structure density. These effects contributed notably to increased RS content. Interestingly, the formation of the V6-type crystalline structure within the complexes was primarily facilitated by the CH-π interaction between the aromatic rings of RA and the C-H of starch, rather than conventional hydrogen bonding and electrostatic forces. The strength of the CH-π interaction increased with higher amylose content and lower molecular weight of the starch, achievable through a 12-h pullulanase hydrolysis followed by a 2-h α-amylase hydrolysis. The resulting HPH-Pα2-RA complexes exhibited remarkable levels of the V-type crystalline structure and RS content, reaching up to 25.45% and 57.37%, respectively. Overall, this study offers valuable insights into the design of starch-polyphenols complexes with a high RS content.

Keywords: Starch-resveratrol complexes; CH-π interactions; High-pressure homogenization; *In vitro* digestibility; Ordered structures

1 Introduction

In recent years, resistant starch (RS) has gained recognition as a vital dietary fiber component with promising nutritional benefits. A novel approach to boost RS content and enhance its nutritional advantages is the creation of starch-polyphenols complexes (Deng, et al., 2021). Among these, stilbene polyphenols have taken the spotlight due to their remarkable π-plane conjugation, contributing to enhanced stability and antioxidant properties (Wu, et al., 2021). This makes them ideal candidates for forming complexes with starch.

Research has shown that starch and polyphenols can create non-covalent complexes, such as non-inclusion complexes and V-type inclusion complexes, through various molecular interactions such as hydrogen bonding and hydrophobic interactions (Gutierrez & Bello-Perez, 2022). These interactions can lead to the development of new ordered structures that enhance digestibility. Within this process, one critical factor in formatting starch-polyphenols complexes and unlocking their nutritional potential lies in the structure and physical properties of polyphenols (Giuberti, Rocchetti, & Lucini, 2020). However, stilbene polyphenols exhibit extensive π-plane conjugation and weak hydrophilicity, setting them apart from polyphenols like flavonoids and phenolic acids. Consequently, the interactions within starch-stilbene polyphenols complexes may differ from traditional interactions, and their precise nature remains unclear. Further exploration is needed to clarify these interactions, ultimately paving ways for the design of starch-polyphenols complexes with elevated RS content.

Another pivotal determinant is the molecular structure of starch. In contrast to amylopectin, amylose, characterized by both lower molecular weight (M_w) and linear characteristics, exhibits

a greater affinity for complexing with guest molecules (Amoako & Awika, 2016). Therefore, the amylose content and M_w of starch play significant roles in shaping the interactions between starch and polyphenols, ultimately impacting digestibility (Barros, Awika, & Rooney, 2012).

To leverage the advantages of interactions between high amylose starch and polyphenols, researchers have explored enzymatic modification as a means of modifying starch molecular chains. Among these enzymes, pullulanase stands out for its ability to selectively break α-1,6 glycosidic bonds, thus increasing the amylose content (Wang, Nie, & Xu, 2019). On the other hand, α-amylase contributes by randomly hydrolyzing internal α-1,4 glycosidic bonds, reducing the M_w (Evans, van Wegen, Ma, & Eglinton, 2003). It is worth noting that the combinational use of pullulanase and amylase can simultaneously elevate amylose content and reduce M_w, achieving precise control over the ordered structure and digestibility of starch (Guo, et al., 2022).

However, the study of co-utilizing pullulanase and α-amylase to synergistically hydrolyze starch and its consequential impact on interactions between the hydrolyzed starch and polyphenols, especially stilbene polyphenols, remains largely unexplored. To design starch-stilbene polyphenol complexes with elevated RS content, it is crucial to delve into the underlying mechanisms governing the complexation between stilbene polyphenols and high amylose starch with different M_w.

Thus, in this study, we began by employing pullulanase and α-amylase to collaboratively hydrolyze high-amylose corn starch (G50). We examined the effect of different hydrolysis durations on amylose content and M_w. Then, we selected resveratrol (RA), a representative stilbene polyphenol with a typical stilbene structure (Chen, et al., 2022). The formation of

starch-RA complexes was achieved through high-pressure homogenization (HPH). It is reported that HPH causes the degradation of starch molecules and increases the amylose content by destroying starch particles and narrowing the size distribution of starch molecules, facilitating interactions between starch molecules and ligands to form complexes (Zhao, Wang, Zheng, Chen, & Guo, 2019). Through an examination of the key structural characteristics of starch-RA complexes formed under HPH, we investigated how amylose content and M_w influence the structure and digestibility of these complexes. Building upon this foundation, we further studied the intermolecular non-covalent interactions within starch-RA complexes through NMR and quantum chemistry analyses. The comprehensive investigation aims to provide valuable insights for the design of starch-polyphenols complexes with enhanced health benefits.

2 Materials and methods

2.1 Materials

The G50 starch, with an amylose content of 50%, was commercially sourced from Penford Australia Ltd. (Jannali, NSW, Australia). Its amylose content was verified following our previous work (Zou, et al., 2012) using iodine-binding of AACC method 61-03, with modifications employing spectrophotometric detection (Tan, et al., 2017). The M_w of G50 was determined using gel permeation chromatography (GPC) coupled with multi-angle light scattering (MALS) as outlined in **section 2.4.2**. Resveratrol (RA) of food-grade purity was procured from Shaanxi Senfu Biotechnology Co., Ltd (China). Porcine pancreas-derived α-amylase (activity: ≥5 U/mg) and amyloglucosidase (activity: 100 U/mg) were sourced from

Sigma (USA). Analytical-grade reagents were obtained from Macklin (China) and Sigma (USA).

2.2 Sample preparation

2.2.1 Pre-enzymatic modification

As previously reported, the pre-enzymatic modification process was conducted with minor modifications (Liu, Kang, et al., 2019). First, a 10 wt.% (dry basis) G50 starch solution was prepared in a three-necked flask and gelatinized for 1 h at 115 °C. Then, 140 U/g of pullulanase was added to the gelatinized G50 paste for enzymatic hydrolysis, conducted at 55 °C (pH = 5.5) for 8 h, 12 h, or 16 h. Following enzymatic hydrolysis, the resulting precipitate was dispersed at a ratio of 1:4 (precipitate/absolute ethanol) and subjected to centrifugation thrice for 5 min each time. Finally, the precipitates were dried overnight and sifted through a 100-mesh sieve. These samples were denoted as P-8h, P-12h, and P-16h, respectively.

For subsequent processing, high-temperature-resistance α-amylase was applied under similar conditions based on our preliminary experiments. The P-12h sample was chosen due to its high amylose content and short enzymatic hydrolysis time. After the pH was adjusted to 5.0, the α-amylase (200 U/g) was added to hydrolyze the starch at 95 °C for 0.75 h or 2 h. The subsequent steps involving centrifugation and drying were consistent with those mentioned above. These samples were designated as P-α-0.75h and P-α-2h, respectively.

2.2.2 Preparation of HPH samples

The preparation of HPH samples was according to our previous method of HPH-G50 complexes with some modifications (Yang, Guo, Li, Chen, & Zheng, 2024). First, a starch

sample was prepared with a starch concentration of 6.0 wt.% (10 g dry basis) and subjected to gelatinization at 115 °C for 1 h. Then, 3% (w/w, based on 10 g starch dry basis) of RA was dissolved in 2 mL of ethanol and added to the starch paste, which was further gelatinization at 115 °C to remove the ethanol. The mixtures underwent homogenization at 150 MPa using an ultra-high-pressure nano-homogenizer, conducted three times.

Next, 30% ethanol was added according to the volume ratio of 2:1 (starch/ethanol). The mixture was then centrifuged for 5 min to remove any free RA. After undergoing a 24 h freeze-drying process, the sample was crushed through a 100-mesh sieve to obtain different samples. The HPH samples were labeled as HPH-P8-x, HPH-P12-x, HPH-P16-x, HPH-Pα0.75-x, and HPH-Pα2-x, respectively, where P8, P12, and P16 represented the starch with pullulanase hydrolysis time of 8 h, 12 h and 16 h as well as Pα0.75 and Pα2 represented the starch with pullulanase hydrolysis time of 12 h and further α-amylase hydrolysis time of 0.75 h and 2 h. Moreover, x represented the presence or absence of RA in the samples.

2.3 Molecular chain structures

2.3.1 Amylose content

Amylose content was determined using the iodine-binding method described in AACC method 61-03, with adjustments made for spectrophotometric detection (Tan, et al., 2017). The amylose content was quantified based on the absorbance value at 620 nm, referencing a standard curve.

2.3.2 Molecular weight

The molecular weight (M_w) of the samples was determined using a GPC system coupled

with a MALS detector (632.8 nm, DAWN HELEOS, Wyatt Technology, Santa Barbara, CA, USA) and a refractive index (RI) detector (Optilab rex, Wyatt Technology), as detailed in our earlier publication (Qiu, Zeng, Xu, Zheng, & Chen, 2023).

2.4 Complex indexes (*CI*)

The determination of *CI* followed the procedure outlined in a previous publication (Lin, Hu, Huang, Lin, & Yen, 2020). To perform the measurement, 1 g of HPH starch-RA complexes was mixed with 9 mL of ethanol and centrifuged for 5 min at 8000 r/min. Then, 1 mL of the supernatant was transferred into a 25 mL colorimetric tube, to which 5 mL of $FeCl_3$-$K_3[Fe(CN)_6]$ reagent was added, and the mixture was then diluted to 25 mL. The absorbance at 760 nm was recorded using a UV-2600 spectrophotometer (Shimazu, Japan) and calculated using the following formula:

$$CI = \frac{A_c - A_t - A_b}{A_c} \times 100\% \quad (1)$$

A_c, A_b, and A_t were the absorbance of RA, the HPH starch sample, and the HPH starch-RA complexes, respectively.

2.5 *In vitro* digestibility

The measurements of rapidly digestible starch (RDS), slowly digestible starch (SDS), and resistant starch (RS) were conducted following the procedure outlined in our previous study (Zeng, Zheng, Li, & Chen, 2022). Additional details are provided in the supporting information.

$$\mathrm{RDS} = (G_{20} - \mathrm{FG}) \times 0.9 \quad (2)$$

$$\mathrm{SDS} = (G_{120} - G_{20}) \times 0.9 \quad (3)$$

$$\mathrm{RS} = \mathrm{TS} - (\mathrm{RDS} + \mathrm{SDS}) = \mathrm{TS} - (G_{120} \times 0.9) \quad (4)$$

FG represents the initial quantity of glucose available at the start of digestion, precisely at

the 0 min mark. Similarly, G_{20} and G_{120} denote the quantities of glucose released during digestion at the 20 min and 120 min intervals, respectively. Additionally, TS means the total starch content.

2.6 RA release assay

RA release assay during digestion was measured by the Folin-Ciocalteu method according to the previous study (Stojanovic et al., 2012). Additional details are provided in the supporting information.

2.7 Ordered structures

The assessment of short-ordered structures in the samples was conducted using a Fourier-transform infrared (FTIR) spectrometer (Bruker, Germany). The examination employed an attenuated total reflection (ATR) single-reflection cell (Zheng, Liu, Chen, Qiu, & Li, 2022) with 64 scans over the range of 4000 cm^{-1} to 400 cm^{-1}.

The investigation of helical structures in the samples was carried out using a solid-state carbon-13 nuclear magnetic resonance (^{13}C NMR) spectrometer, specifically Bruker AVANCE III HD 400 spectrometer (Bruker, Germany), with a total of 1600 scans (Zheng, Wang, Wang, Chen, & Zhou, 2020).

To assess the crystalline structures of the samples, X-ray diffractometry was employed (PANalytical Co., Almelo, Netherlands), covering an angle from 5 to 45°, with a scan speed of 10°/min. (Zheng, et al., 2020).

For the examination of aggregate structures in the samples, small-angle X-ray scattering (SAXS) analysis was performed (PANalytical Co., Almelo, Netherlands), equipped

monochrome Cu-K radiation with a wavelength of 0.1542 nm (Iiyama, Ruike, & Kaneko, 2000; Qiu, Zheng, Xu, Chen, & Chen, 2022). Additional details can be found in the supporting information.

2.8 DSC analysis

The differential scanning calorimetry (DSC) 8000 instrument (Perkin Elmer, USA) was utilized to measure the enthalpy change (ΔH) during the phase transition, at a rate of 10 °C/min from 10 °C to 140 °C (Zhang, Zheng, Du, Chen, & Chen, 2023).

2.9 Hydrogen bonding interaction

OMNIC 8.0 software was used for the analysis of the region of 1200–800 cm^{-1} in the ATR-FTIR spectra. The settings for the half bandwidth and enhancement factor were 19 cm^{-1} and 1.9, respectively (Qiu, Chen, Rao, & Zheng, 2023).

2.10 Proton flexibility

Proton flexibility analysis was performed using an Advance III 500 MHz Bruker NMR spectrometer (Bruker Corporation, Billerica, USA), following a previously reported method (Li, Ndiaye, Corbin, Foegeding, & Ferruzzi, 2020). Accurately 1 mg of starch sample was weighed and placed into a high-temperature resistant nuclear magnetic tube, along with 0.5 mL of D_2O (TMSP as internal standard). The mixture was heated at 110 °C for 30 min. The test involved a resonance frequency of 64 scans at 70 °C. Proton flexibility was calculated using the following formula:

$$\text{Proton flexibility} = \frac{A_1}{A_0} \times 100\% \quad (5)$$

A_1 and A_0 represent the peak shift integration area of the hydrogenation degree of HPH

samples with and without RA, respectively. These values were normalized using the peak shift integration area of the hydrogenation degree of the internal standard TMSP.

2.11 Quantum chemistry

Density functional theory (DFT) calculations were utilized to provide deeper insights into the interactions between starch and RA. A V6h-type helix model, consisting of six glucose units, was constructed using the CCDC website. The optimization of single and complex structures was carried out using the M06-2x/6–311++G(d,p)/DFT-D3 basis (Frisch, et al., 2016; Grimme, Antony, Ehrlich, & Krieg, 2010). The distribution of electrostatic potential (ESP) was plotted using the Multiwfn software (Zhang & Lu, 2021). To explore these interactions further, the Genmer program generated 100 random conformations of the V6h-type helix-RA complex, which were then optimized using the semiempirical algorithm of the Molclus program (Lu & Chen, 2012). The initial complex structure was further optimized using the same DFT basic set to attain the minimum energy configuration. To evaluate and illustrate noncovalent interactions between molecules, independent gradient model Hirshfeld partition (IGMH) analysis was performed using the Multiwfn software (Lu & Chen, 2022). Visualization of these interactions was facilitated using the VMD software.

2.12 Statistical analysis

The data was presented as the mean ± standard deviation. Statistical analysis, including Duncan's multiple range tests and variance (ANOVA), was performed using SPSS 23 software, with a significance level of $p < 0.05$.

3 Result and discussion

3.1 Molecular chain structures

First, the amylose content and the M_w of enzymatic modified starch were determined. As shown in **Table 1**, compared with G50 (with an amylose content of 51.03%), the amylose content in P-8h (the starch treated with pullulanase for 8 h) significantly increased to 63.92%. With the extension of hydrolysis time, the amylose content in P-16h continued to rise, reaching 84.46%. This indicates that pullulanase specifically hydrolyzes the α-1,6-glucosidic bond of starch, leading to the degradation of amylopectin side chains into shorter amylose chains, thus increasing the amylose content (Wang, et al., 2019).

To further generate starch samples with varying M_w, α-amylase was introduced following a 12-h hydrolysis with pullulanase. The results showed that the amylose contents of P-α-0.75h and P-α-2h were similar to that of P-12h, indicating that the additional application of α- amylase did not alter their amylose contents. In **Table 1**, the M_w of G50 was 2.59×10^7 g/mol, with a concentrated molecular weight distribution exceeding 5×10^5 g/mol. As the hydrolysis time with pullulanase extended, the M_w of P-8h and P-16h decreased from 9.359×10^6 g/mol to 5.906×10^6 g/mol, with the majority of molecular weight distribution falling below 5.0×10^5 g/mol. Furthermore, the M_w underwent a significant reduction following the addition of α-amylase. The M_w of P-α-2h decreased to 0.69×10^5 g/mol, predominantly distributed within the range of $2.0 \times 10^4 – 5.0 \times 10^4$ g/mol. This reduction was attributed to the effective breaking of α-1,4-glucoside bonds in the starch system by α-amylase, resulting in a decrease in M_w and a shift toward a lower molecular weight distribution. These findings demonstrate the successful

regulation of amylose content and M_w of G50 by controlling the durations of hydrolysis by pullulanase and α-amylase.

Table 1. Molecular weight and distribution of the starch samples.

Samples	amylose content (%)	M_w (× 10^5 g/mol)	<2×10^4 (%)	2-5×10^4[a] (%)	5×10^4[a]-1×10^5[a] (%)	1-5×10^5[a] (%)	5×10^5[a]-1×10^6[a] (%)	>1×10^6[a] (%)
G50	50.03±0.11[e]	25.92	0	0	0	0	47.15	52.82
P-8h	63.92±0.84[d]	9.359	0.11	0.24	1.15	11.14	52.25	35.11
P-12h	78.42±0.45[b]	8.325	0.72	1.20	8.65	15.12	50.06	24.25
P-16h	84.46±0.61[a]	5.906	1.94	4.31	16.50	22.14	41.25	13.86
P-α-0.75h	77.56±0.74[b]	2.148	3.12	15.02	18.72	45.48	16.23	1.43
P-α-2h	76.42±0.69[b]	0.697	16.70	36.16	31.44	15.00	0.70	0
HPH-P8	66.33±0.56[c]	5.721	0.24	1.45	5.67	33.55	30.26	28.83
HPH-P12	80.34±0.45[b]	5.543	0.98	3.23	14.06	16.32	44.76	16.65
HPH-P16	85.32±0.44[a]	5.291	2.78	7.34	18.55	24.69	36.32	10.32
HPH-Pα0.75	77.49±0.71[b]	1.901	4.54	18.34	23.99	40.67	12.46	0
HPH-Pα2	76.88±0.75[b]	0.693	18.33	43.48	25.87	12.32	0	0

[a] g/mol; Values are presented as means ± SD; The different letters were significantly different ($p < 0.05$).

Then, the amylose content and the M_w of starch samples after HPH treatment were determined. As shown in **Table 1**, compared with enzymatic modified starch, the amylose content in HPH treated samples slightly increased to 66.99%-85.76%, due to high-speed shear during HPH treatment could degrade the starch molecule to release more amylose (Liu, Chen, Xu, Liang, & Zheng, 2019). In **Table 1**, the M_w of HPH-P8 to HPH-P16 showed a significant reduction during HPH treatment, demonstrating the branches of amylopectin and long chains of amyloses were fractured during the HPH process. However, the M_w of HPH-Pα-0.75 and HPH-Pα-2 unchanged, which could be attributed to the addition of α-amylase reaching a definite minimum chain length to limit the degradation process caused by shear (Wang, Li,

Wang, Liu, & Adhikari, 2012). The results (**Table S1**) also showed that the complexation with RA during HPH treatment did not alter the amylose contents and M_w of HPH starch-RA complexes.

3.2 *CI*

As shown in **Table 2**, as the hydrolysis time with pullulanase was extended, the *CI* values of HPH-P-RA complexes increased from 59.67% to 65.67%, respectively. These values were significantly higher than HPH-G50-RA ($p < 0.5$). This increase can be mainly attributed to the hydrolysis of the starch's 1,6-glycosidic bond by pullulanase, resulting in a reduction in the content of amylopectin and an increase in amylose content. This, in turn, led to a decrease in steric hindrance during the interaction (Barros, et al., 2012) between the starch and RA under HPH conditions.

The *CI* values of HPH-Pα0.75-RA and HPH-Pα2-RA further increased to 76.33% and 86.00%, respectively. This was mainly due to the hydrolysis of the starch's 1,4-glycosidic bonds by α-amylase, facilitating the production of low-molecular-weight amylose molecules. This enhancement promoted the formation of complexes between RA and the starch, resulting in increased *CI* values.

3.3 *In vitro* digestibility

As shown in **Table 2**, the addition of RA under HPH conditions significantly increased the RS content. The HPH-P-RA complexes presented lower RDS content and higher RS content with increasing enzymatic hydrolysis time. This phenomenon is linked to the rise in amylose content and the reorganization of starch molecular chains (Liu, Chen, & Zheng, 2022). The

279 increased amylose content contributed to enhanced aggregation and rearranged crystallinity,
280 ultimately improving starch digestibility (Wang, et al., 2023). Compared to HPH-P12-RA,
281 HPH-Pα-RA demonstrated a notably higher RS content ($p < 0.5$), indicating increased
282 resistance to digestibility as M_w decreased. This can be attributed to the increased short amylose
283 content enhancing the interaction between the starch and RA (as shown by the increased *CI*),
284 which enhanced structural order (Guo, et al., 2022). Specifically, HPH-Pα0.75-RA and HPH-
285 Pα2-RA achieved RS contents of 54.53% and 57.37%, respectively, demonstrating that the
286 addition of α-amylase during HPH promoted the formation of starch-RA complexes with higher
287 RS content.

288 Since the phenolic compound like RA is known to inhibit the enzyme activity for starch
289 digestion by blocking the reaction center of the enzyme, the released content of RA from
290 complex and the digestibility of simple mixtures of HPH with corresponding released RA were
291 further studied. The RA release results demonstrated that only a small amount of RA dissociated
292 from the complex during digestion within the first 20 min (**Figure S1**). This is reasonable due
293 to most of the free RA being washed away after preparation of HPH-RA complexes. Meanwhile,
294 as shown in **Table S2**, the RS contents of simple mixtures of HPH samples with corresponding
295 released RA showed a slight increase (below 3%), indicating that few dissociated RA could act
296 as an enzyme inhibitor to reduce the digestibility (Cao, Zheng, Zeng, & Chen, 2024). Therefore,
297 the increased RS of HPH-RA complexes primarily came from the formation of anti-enzymatic
298 structures. To gain deeper insights into these structural changes, the key multi-scale structural
299 changes of HPH samples were studied, as discussed below.

300 **Table 2**. Complex indexes (*CI*) and digestibility of the high-pressure homogenization (HPH) samples

Samples	*CI* (%)	RDS (%)	SDS (%)	RS (%)
HPH-G50-RA	58.67±0.03^{f}	-	-	-
HPH-P8	-	65.75±0.25^{a}	11.03±0.06^{cd}	23.22±0.31^{j}
HPH-P8-RA	59.67±0.06^{e}	58.44±0.45^{b}	6.73±0.39^{g}	34.83±0.84^{g}
HPH-P12	-	57.34±0.60^{c}	12.15±0.77^{b}	31.10±0.79^{i}
HPH-P12-RA	62.11±0.03^{d}	43.37±0.63^{f}	9.34±0.69^{e}	47.24±0.78^{d}
HPH-P16	-	55.15±0.12^{d}	14.07±0.10^{a}	30.78±0.21^{h}
HPH-P16-RA	65.67±0.10^{c}	41.74±0.24^{f}	10.14±0.11^{f}	48.12±0.13^{c}
HPH-Pα0.75	-	49.74±0.26^{e}	13.36±0.66^{a}	36.90±0.74^{f}
HPH-Pα0.75-RA	76.33±0.18^{b}	42.22±0.27^{f}	3.25±0.25^{i}	54.53±0.19^{b}
HPH-Pα2	-	49.80±0.45^{e}	11.80±0.48^{bc}	38.40±0.05^{e}
HPH-Pα2-RA	86.00±0.24^{a}	32.81±0.69^{g}	9.82±0.79^{ef}	57.37±0.19^{a}

301 Values are presented as means ± SD; The different letters were significantly different ($p < 0.05$).

302 **3.4 Short-range ordered structures**

303 The surface short-range ordered structure of the starch samples closely correlated with
304 changes in characteristic peaks at 1047 cm^{-1} and 1022 cm^{-1} in ATR-FTIR spectra (Wang, Wang,
305 Guo, Liu, & Wang, 2017). As shown in **Figure 1A**, there was no discernible RA characteristic
306 absorption peak in the spectra, confirming the absence of free RA molecules. **Figure 1B** and
307 **Table 3** reveal that the addition of RA significantly increased the $R_{1047/1022}$ value for HPH starch-
308 RA complexes, indicating that RA promoted the formation of short-range ordered structures
309 through non-covalent interactions with the starch. In the case of HPH-P-RA complexes,
310 $R_{1047/1022}$ increased with prolonged pullulanase hydrolysis duration. Pullulanase augmented the
311 amylose content, enhancing interactions between the starch and RA under HPH conditions and
312 consequently improving short-range ordered structures. Notably, compared to the HPH-P12-
313 RA complexes, the $R_{1047/1022}$ values for HPH-Pα-RA complexes further increased. The

hydrolysis by α-amylase significantly reduced the starch's M_w, making it more conducive to non-covalent interactions like hydrogen bonding with RA, further enhancing short-range ordered structures.

3.5 Helical structures

In ^{13}C CP/MAS NMR analysis of the starch, specific chemical shifts observed at 94-105 ppm and 81-84 ppm were employed to detect C1 and C4 peaks, respectively, which are indicative of the helical structures of the complexes (Gidley & Bociek, 1988). As shown in **Figure 1C**, the C1 resonance at 103.3 ppm for HPH samples is suggestive of a packing of 6 glucosyl units-fold helices (Biais, Le Bail, Robert, Pontoire, & Buleon, 2006), even following the addition of RA. This indicates that RA, with its linear and compact molecular configuration, could enter the spiral cavity of starch without causing a change to the helical structure.

Table 3 reveals that the inclusion of RA results in an increased single helix content and a decreased double helix content in the HPH-starch-RA complexes. This suggests that under the influence of heat and pressure during HPH, RA is driven into the hydrophobic spiral cavity of starch, increasing the single helix content while impeding the formation of double helices of starch.

Regarding HPH-P-RA complexes, there was an increase in the intensity of the characteristic peak at 103.3 ppm as the pullulanase hydrolysis time extended. This observation indicates that the increased amylose content promoted the formation of single helix structures involving RA and starch. Meanwhile, the rearrangement and aggregation of starch chains were bolstered by the increased amylose content, leading to a higher double helix content within

335 HPH-P-RA complexes.

336 Furthermore, HPH-Pα-RA complexes exhibited elevated levels of single helix and double
337 helix contents than the HPH-P12-RA complexes. This distinction could be attributed to the
338 lower M_w of the starch, which reduced the overall steric hindrance effect within the system.
339 This reduction enhanced the mobility of starch molecular chains (Hou, et al., 2020). On one
340 hand, the shorter starch chains facilitated RA's entry into the spiral cavity of amylose, prompting
341 the formation of single helices. On the other hand, the shorter starch molecular chains
342 transitioned more readily from a disorganized state to an organized one through hydrogen
343 bonding, thus facilitating the creation of double helices.

344 **Table 3.** Key multi-scale structural parameters of the HPH samples.

Samples	$R_{1047/1022}$	Single helix (%)	Double helix (%)	V-type (%)	B-type (%)	α/D_m	Σ (nm)
HPH-P8	0.63±0.01^{g}	6.67±0.12^{j}	19.23±0.21^{f}	6.14±0.10^{i}	17.99±0.17^{f}	1.51±0.02^{f}	3.31±0.02^{a}
HPH-P8-RA	0.71±0.01^{e}	17.27±0.19^{e}	13.68±0.10^{i}	15.68±0.09^{e}	12.07±0.10^{j}	1.58±0.03^{f}	2.99±0.01^{b}
HPH-P12	0.62±0.01^{g}	8.11±0.13^{i}	24.67±0.15^{d}	6.88±0.10^{h}	23.10±0.07^{d}	1.91±0.01^{e}	2.76±0.04^{c}
HPH-P12-RA	0.75±0.01^{d}	20.43±0.22^{d}	15.15±0.13^{h}	20.55±0.50^{d}	13.68±0.07^{i}	2.11±0.04^{d}	2.30±0.02^{e}
HPH-P16	0.66±0.01^{f}	9.04±0.13^{h}	25.31±0.14^{c}	7.24±0.07^{g}	24.17±0.09^{c}	1.95±0.03^{e}	2.64±0.01^{d}
HPH-P16-RA	0.75±0.01^{d}	21.41±0.19^{c}	16.83±0.11^{g}	21.19±0.06^{c}	14.08±0.08^{h}	2.17±0.01^{d}	2.24±0.02^{f}
HPH-Pα0.75	0.77±0.01^{c}	10.24±0.13^{g}	29.66±0.14^{b}	9.12±0.05^{f}	28.61±0.04^{b}	2.23±0.02^{c}	1.90±0.09^{g}
HPH-Pα0.75-RA	0.84±0.01^{b}	23.58±0.12^{b}	19.85±0.11^{e}	22.67±0.06^{b}	16.53±0.09^{g}	2.32±0.04^{b}	1.65±0.03^{h}
HPH-Pα2	0.83±0.01^{b}	11.55±0.13^{f}	30.42±0.08^{a}	9.37±0.13^{f}	30.52±0.10^{a}	2.35±0.06^{ab}	1.47±0.06^{i}
HPH-Pα2-RA	0.96±0.01^{a}	25.53±0.17^{a}	19.56±0.16^{ef}	25.45±0.10^{a}	18.42±0.10^{e}	2.41±0.03^{a}	1.32±0.05^{j}

345 Values are presented as means ± SD; The different letters were significantly different ($p < 0.05$).

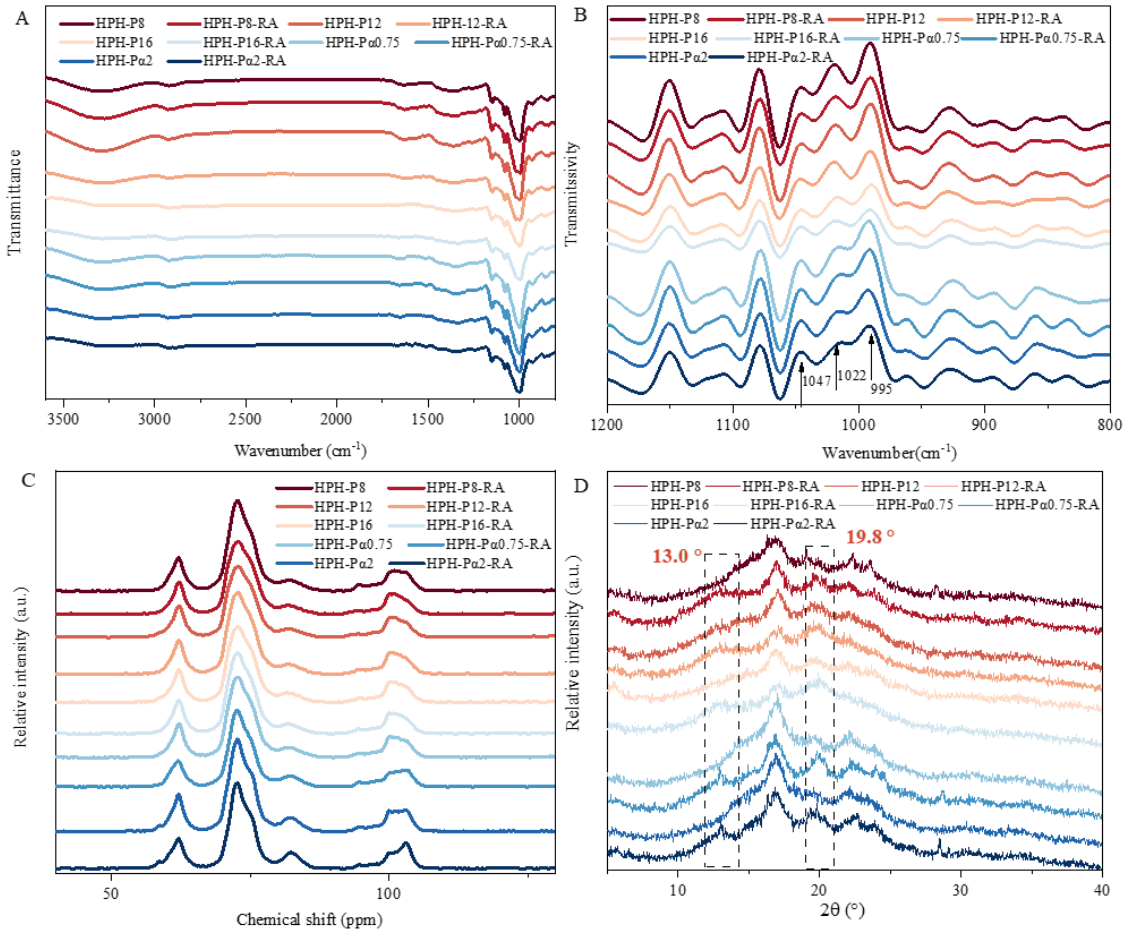

Figure 1. Infrared spectroscopy (A), second derivative infrared spectroscopy (B), ^{13}C CP/MAS NMR (C), and X-ray diffraction (D) results of the HPH samples.

3.6 Crystalline structures

As depicted in **Figure 1D**, all samples exhibited major diffraction peaks at $2\theta = 17.1°$, 22.2°, and 24.0°, characteristic of the typical B-type crystalline structure. Additionally, V-type diffraction peaks at 13.0° and 19.8° were observed, corresponding to the V6-type crystalline structures as previously reported (Kong, Lee, Kim, & Ziegler, 2014). When comparing HPH samples with and without RA, it was evident that the major diffraction peaks remained consistent for HPH-starch-RA complexes. This indicates that the addition of RA did not change the V6-type structures, likely due to their limited spatial hindrance (Yang, et al., 2024).

On one hand, the B-type diffraction peaks showed reduced intensity, attributed to RA

hindering the formation of double helices through starch interactions (Zeng, et al., 2022). On the other hand, the V6-type diffraction peaks, particularly the peak at $2\theta = 19.8°$, for HPH-starch-RA complexes became more distinct. According to a previous report, the peak at $2\theta = 19.8°$ signifies the presence of a semi-crystalline (type II) intrahelical V-type crystalline structure with enhanced order. This increased order arises from the structured complexation of single amylose helices with guest molecules (Lopez-Rubio, Flanagan, Gilbert, & Gidley, 2008).

In the case of HPH-P-RA complexes, the V-type crystalline content increased proportionally with the rising amylose content. This increase promoted the formation of single helices within starch-RA complexes, ultimately leading to the formation of the V-type crystalline structure through oriented stacking. Moreover, the relative crystallinity (RC) of HPH-Pα-RA complexes exceeded those of HPH-P12-RA complexes, aligning with the observed trend in helical structures. Specifically, regarding the V-type crystalline structure, the content of V-type crystallinity in HPH-Pα 0.75-RA and HPH-Pα2-RA reached notably high levels, 22.67% and 25.45%, respectively. The reduced M_w of starch chains played a significant role in enhancing the orientation rearrangement (Cui, et al., 2024), resulting in increased double helix and single helix contents and the subsequent development of B-type and V-type crystalline structures under HPH conditions. Based on the increased amylose content of pullulanase, α-amylase could further produce more amylose with a low molecular weight that was suitable to form V-type complexes with RA, leading to the enhancement of the diffraction intensity (Liu, et al., 2020).

3.7 Aggregated structures

SAXS logarithmic plots provide insights into the microstructure of aggregated structures in starch systems. The power-law model $I \sim q^{-\alpha}$ was used to linearly fit SAXS spectra on a logarithmic coordinate axis, yielding α values for HPH samples, which can serve as a measure of gel density (Zheng, et al., 2022). As indicated in **Table 3**, all HPH samples exhibited $D_m(\alpha)$ values below 3, characteristic of a typical mass fractal structure. The SAXS spectra (**Figures 2A**) were transformed into Kratky scattering curves (**Figures 2B**) and Debye-Bueche-power-law SAXS fit curves (**Figures 2C**) to extract the correlation length Σ, which pertains to the submicroscopic gel structure of starch (Zhang, Li, Janaswamy, Chen, & Chi, 2020). As shown in **Figure 2B**, scattering peaks appeared at $q = 0.4$ nm^{-1} for all samples, indicating heterogeneity at the submicroscopic scale. Upon the addition of RA, the D_m value of HPH-starch-RA complexes increased, concomitant with decreasing Σ values. These observations indicate that the interaction between the starch and RA led to the formation of more ordered structures, such as the V-type II crystalline structure, resulting in a denser network system.

With pullulanase hydrolysis, the D_m values of HPH-P-RA complexes increased, while Σ values decreased. The elevation in amylose content promoted the formation of additional starch-RA complexes during the HPH process, thereby enhancing the overlapping density between starch molecular chains. This increase in amylose content also favored the development of single helices and the V-type crystalline structure, contributing to a denser network system. In contrast to HPH-P12-RA, the D_m values of HPH-Pα-RA complexes showed further increases alongside lower Σ values. This suggests that reducing the M_w of the starch

facilitated the enhancement of helical structures and the formation of the V-type II crystalline structure in conjunction with RA, as mentioned above. As a result, these aggregated structures further increased the density of the network system.

3.8 Ordered structures

To gain insight into the ordered structure, the thermal properties of HPH samples were examined using DSC. **Figure 2D** displays two distinct phase transition peaks spanning the temperature ranges of 59-74 °C and 100-130 °C, corresponding to the fusion of B-type and V-type crystalline structures, respectively. As shown in **Table 4**, the introduction of RA did not after T_{p1} but significantly reduced ΔH_1. This reduction was attributed to the formation of hydrogen bonding between RA and the starch, which impeded the interaction between starch chains, thus inhibiting the formation of double helices and the B-type crystalline structure, as discussed earlier. Moreover, the addition of RA increased the T_{p2} from 95-105 °C (observed in HPH-starch samples) to 121-125 °C (observed in HPH-starch-RA complexes) while increasing ΔH_2. This shift indicates that starch-RA complexes promoted the development of dense and the ordered V-type II crystalline structure (Chao, Yu, Wang, Copeland, & Wang, 2018) during the HPH process. Essentially, the linear ligands of RA allowed them to reside exclusively within the helical cavities, resulting in a compact crystalline structure (Deng, et al., 2021).

In the case of HPH-P-RA complexes, their ΔH_1 and ΔH_2 values exhibited an increase corresponding to higher amylose content. This increase resulted from the formation of more starch-RA complexes, leading to an overall enhancement of the ordered structure during the HPH process. Compared to the HPH-P12-RA complexes, the ΔH_2 values of HPH-Pα-RA

complexes increased, while the ΔH_1 values decreased. This observation suggests that short amylose molecules resulting from amylase hydrolysis not only strengthened the hydrogen bonding interaction with RA, thereby increasing the V-type crystallinity but also suppressed the B-type crystalline structure during the HPH process. These findings align with the results of the crystalline structures discussed earlier.

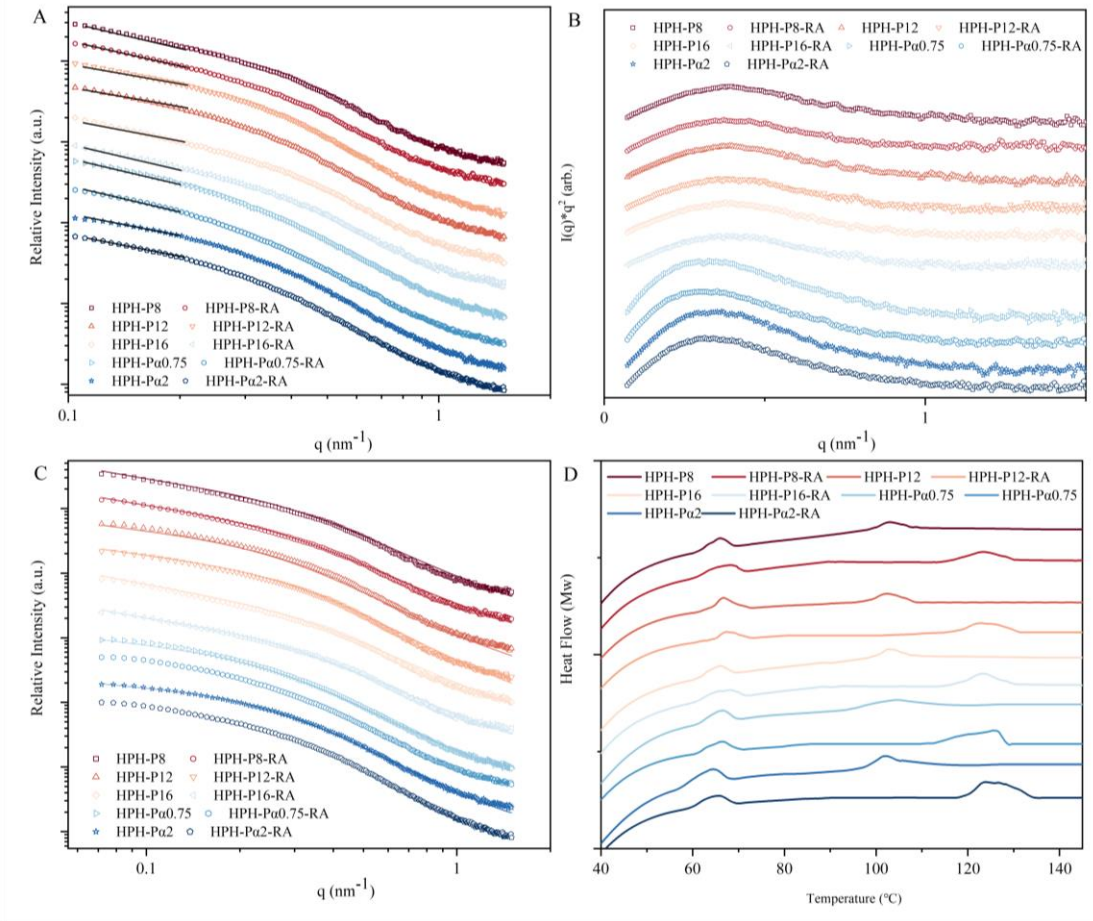

Figure 2. SAXS double logarithmic plots (A), Kratky plots (B), Debye-Bueche-power-law SAXS fit curves (C), and DSC curves (D) of the HPH samples.

3.9 Hydrogen bonding interaction

To further investigate the interactions between the starch and RA, ATR-FTIR spectroscopy was used. In ATR-FTIR spectra, the absorption peak at 998 cm^{-1} is associated with ν-C-O-H and is related to the intramolecular hydrogen bonding involving the C6-OH group on the

glucose unit of starch (Qiu, Chen, et al., 2023). As illustrated in **Figure 3A** and detailed in **Table 3**, the C-O-H stretching vibration (C-O-H def) of HPH starch-RA complexes exhibited a shift to higher wavenumbers compared with HPH starch samples without RA. This shift can be attributed to the addition of RA, which facilitated the formation of single helix structures, thereby enhancing the hydrogen bonding interactions within the starch (Chen, et al., 2020).

Additionally, the C-O-H def of the HPH-P-RA complexes also shifted to higher wavenumbers, indicating that the increased amylose content enhanced the hydrogen bonding interaction between the starch and RA. Notably, the C-O-H def of HPH-Pα0.75-RA and HPH-Pα2-RA exhibited additional shifts to 994.55 cm^{-1} and 996.09 cm^{-1}, respectively. This phenomenon can be attributed to the higher *CI* value of HPH-Pα-RA complexes, resulting from the use of the lower M_w starch produced by α-amylase. This led to a more pronounced enhancement of hydrogen bond interaction.

3.10 Proton flexibility

The above results indicate a substantial enchantment in the RS content of the starch due to the formation of inclusion complexes characterized by single helices and the subsequent stacking of the V-type crystalline structure. Previous research has suggested that the formation of starch-polyphenol inclusion complexes occurs through weak hydrogen bonding, specifically CH-π interaction dominated by van der Waals forces (Jimenez-Moreno, et al., 2015). During this process, C3-H and C5-H of the glucose unit play crucial roles in CH-π interaction formation (Li, et al., 2020), resulting in a reduction in the peak integral area of the chemical shift and limiting proton flexibility (Asensio, Arda, Canada, & Jimenez-Barbero, 2013; Ribeiro, et al.,

2008). To gain further insights into the CH-π interaction within starch-RA inclusion complexes, H proton flexibility was analyzed. The chemical shift at 4.24 ppm for C5-H and C6-H was too close to distinguish reliably. Thus, we focused on C3-H, which exhibited a chemical shift at 4.34 ppm, as the site for evaluating proton flexibility.

Table 4. Thermal parameters, hydrogen bonding interaction parameters, and proton flexibility of the HPH samples

Sample	T_{p1} (℃)	ΔH_1 (J/g)	T_{p2} (℃)	ΔH_2 (J/g)	Peak (cm^{-1})	C3-H (A_{C3-H})	Proton flexibility
HPH-P8	66.72±0.22^{e}	7.35±0.03^{f}	103.14±0.18^{e}	1.62±0.06^{j}	990.41	0.37±0.02^{a}	100%
HPH-P8-RA	67.52±0.24^{bc}	5.73±0.04^{j}	123.93±0.08^{b}	7.26±0.10^{e}	991.85	0.32±0.03^{c}	86.46%
HPH-P12	67.55±0.06^{a}	8.12±0.01^{d}	102.87±0.23^{e}	1.95±0.05^{i}	991.05	0.35±0.01^{b}	100%
HPH-P12-RA	67.34±0.28^{cd}	6.25±0.02^{i}	123.66±0.20^{c}	9.09±0.07^{d}	992.57	0.28±0.02^{d}	80.00%
HPH-P16	67.06±0.15^{de}	8.30±0.03^{c}	102.38±0.22^{f}	2.14±0.04^{h}	991.22	0.30±0.03^{c}	100%
HPH-P16-RA	67.84±0.11^{ab}	6.54±0.04^{h}	122.94±0.26^{c}	9.10±0.06^{c}	992.78	0.23±0.01^{e}	76.76%
HPH-Pα0.75	67.37±0.24^{cd}	8.92±0.05^{b}	104.04±0.21^{d}	3.45±0.05^{g}	992.84	0.31±0.02^{c}	100%
HPH-Pα0.75-RA	66.98±0.24^{e}	7.18±0.04^{g}	127.19±0.36^{a}	10.16±0.04^{b}	994.55	0.23±0.04^{e}	74.19%
HPH-Pα2	65.34±0.23^{f}	9.20±0.03^{a}	102.27±0.27^{f}	3.69±0.05^{f}	994.28	0.30±0.02^{cd}	100%
HPH-Pα2-RA	67.06±0.26^{d}	7.43±0.02^{e}	123.23±0.23^{c}	11.82±0.04^{a}	996.09	0.22±0.03^{e}	73.33%

Values are presented as means ± SD; The letters after the values were significantly different ($p < 0.05$).

Figure 3B reveals that, compared to HPH-starch samples, the addition of RA led to a reduction in the intensity of chemical shift peaks associated with the proton flexibility of C3-H, indicating that the interaction between RA and the starch restricted this proton flexibility on glucose within HPH starch-RA complexes. In the case of HPH-P12-RA complexes, the proton flexibility of C3-H decreased with an increase in amylose content, suggesting an enhanced CH-π interaction between the starch and RA under HPH conditions (**Table 4**). Furthermore, the proton flexibility of C3-H of HPH-Pα-RA complexes was further reduced when compared to HPH-P12-RA complexes. Pa samples with lower M_w were more conducive to the formation of

starch-RA complexes through CH-π interaction, consistent with the observed ordered structures.

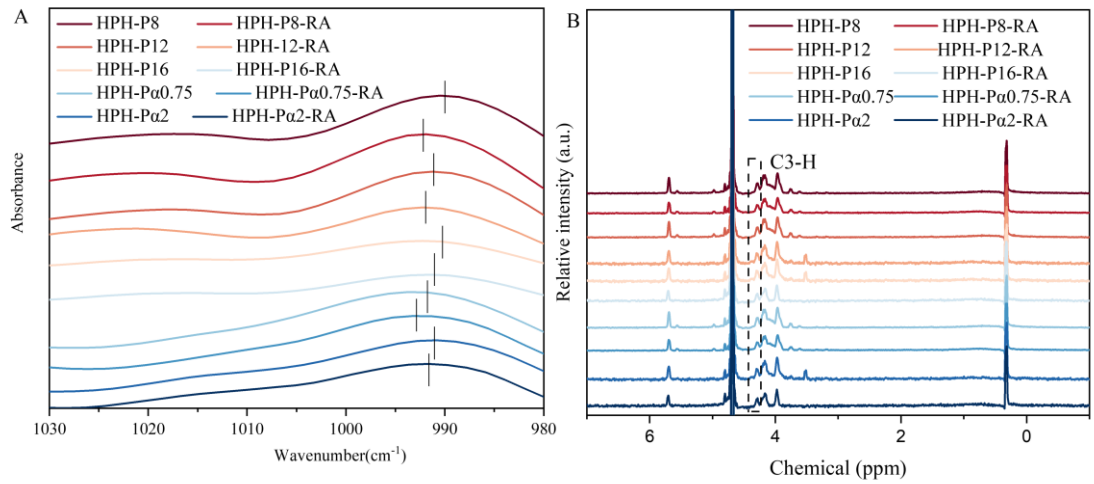

Figure 3. Second derivative infrared spectroscopy (A) and ^{1}H-NMR curves (B) of the HPH samples.

3.11 Quantum chemistry

To further enhance the understanding of C-H-π interaction involved in starch-RA complexes, quantum chemistry was utilized. As mentioned above, the results regarding helical and crystalline structures demonstrate that the single helices of starch-RA complexes could adopt a V6-type configuration with six glucose units per turn. Illustrated in **Figure 4A**, the V6-helices exhibited a somewhat distorted spatial structure, positioning both C3-H and C5-H within the spiral cavity (Wang, et al., 2020) in a configuration of minimum energy due to intramolecular hydrogen bonding. Conversely, the RA molecule displayed an extensive planar π-conjugated molecular configuration without forming intramolecular hydrogen bonds. Electrostatic potential analysis (ESP) was employed to predict and elucidate potential binding sites and strengths of free monomers.

In **Figure 4B**, the ESP revealed maximum and minimum points, represented by the yellow and green spheres, respectively, positioned in proximity to the hydroxyl group or the carboxyl group within a stable configuration. This suggests that these groups serve as the primary sites

for molecular interactions. Moreover, the maximum and minimum points also appeared in the benzene ring of RA, indicating that the conjugated π plane of the RA benzene ring can also function as a potential site for non-covalent interactions.

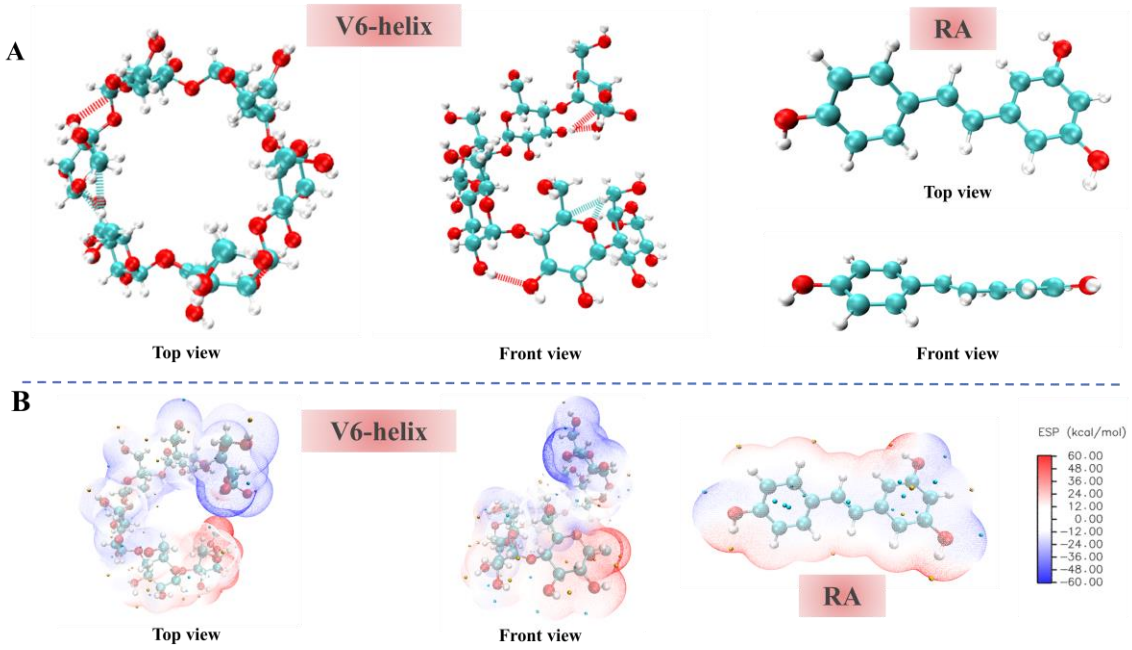

Figure 4. Optimized stable conformer (A) and ESP distribution (B) of the V6-helix and RA.

Subsequently, the stable configuration of V6 helix-RA complexes was optimized while considering an implicit solvation model to simulate the conditions of HPH. In comparison to the individual molecules discussed earlier, the V6-helix in the complex underwent molecular configuration changes, resulting in an increased number of intramolecular/intermolecular hydrogen bonds to maintain energy conservation (**Figure 5A**). It was evident that the active site involved in intermolecular hydrogen bonding within the complexes exhibited similarities to the outcomes of the ESP analysis. These included not only conventional hydrogen bonds, such as O-OH and CH-O (indicated by red dashed lines), but also many new hydrogen bonds associated with CH- π Interaction (indicated by blue dashed line) (Raju, Ramraj, Hillier, Vincent, & Burton, 2009). These interactions mainly occurred between the benzene ring of RA and the C-H group

of the V6-helix.

In **Figure 5B**, the atoms were color-coded based on δG_{atom} to illustrate their contributions to the interaction. According to the color bar, the redder (bluer) color corresponds to larger (smaller) atomic contributions to the complexation between the two atoms. Notably, atoms located at the benzene ring of RA and the C-H groups of the V6-helix exhibited significant contributions. Specifically, the C3-H atoms situated in the vicinity of the glucose units inside the spiral cavity of the V6-helix displayed the most substantial contribution, consistent with the findings from the proton flexibility analysis.

IGMH analysis was utilized to unveil the intermolecular interactions within the V6-helix-RA complex, and sign(λ2)ρ colored δg_{inter} isosurface maps were plotted. The presence of green isosurfaces demonstrates the presence of significant van der Waals interactions, such as CH-π interaction. Additionally, the green patches surrounding blue areas signify the existence of conventional hydrogen bonds, such as O-OH and O-CH bonds. As illustrated in **Figure 5C**, there were green isosurfaces with a few blue regions located between the V6-helix and RA, suggesting the possibility of RA being included into the V6-helix to form the complex based on CH-π interaction instead of conventional hydrogen bonds interaction. Furthermore, the δ_{g_Inter} value between the V6-helix and RA was 1.16 a.u., primarily due to CH-π interaction. The findings revealed that the complexation between RA and the starch relied on the new CH-π interaction rather than traditional hydrogen bonding interaction. This is in line with the results of proton flexibility. Hence, the impact of this on the structure and digestibility of the complex is in agreement with the results outlined in the structural analysis section.

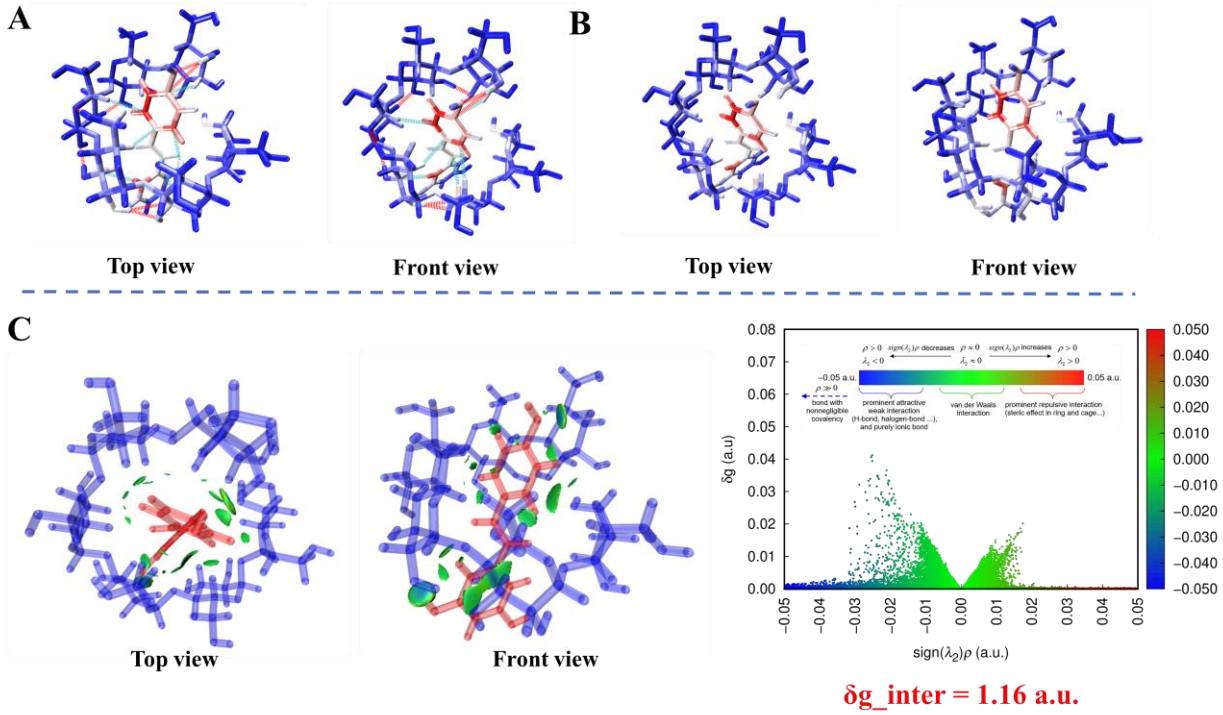

Figure 5. Hydrogen bonding interaction (A) and their atoms are colored by δG_{atom} (B) of the V6-helix-RA complex. IGMH analyses (C) of the V6-helix-RA complex, which is defined by the two fragments.

3.12 Underlying mechanisms of CH-π interaction in altering the structure and digestibility of starch-RA complexes formed via the HPH process

Based on the above findings from *in vitro* digestibility, structural changes, ATR-FTIR, NMR, and quantum chemistry analyses, it has been elucidated that CH-π interaction plays a crucial role in the complexation between RA and the starch with varying M_w (see **Figure 6**). HPH treatment resulted in the quick dispersion of RA in starch paste due to the high-speed shear force, leading to its interaction with starch molecules through non-covalent interactions. The incorporation of RA resulted in a reduction in double helices and the B-type crystalline structure, but increased single helix structure and V-type crystalline structure (V6 II type). These improved single helix and V-type crystalline structures were generated via the inclusion complexation process. Due to the limited space hindrance and the π conjugation structure, RA

can effortlessly enter the starch spiral cavity and create steady inclusion complexes through CH-π interaction controlled by Van der Waals forces. Consequently, there was a more condensed aggregate structure and a more overall ordered structure of the complexes, eventually leading to higher RS.

Breaking the α-1,6-glycosidic bond with pullulanase resulted in an increase in amylose content within the system. Additionally, α-amylase aided in the breakage of the α-1,4-glycosidic bond of starch, thus increasing the low M_w starch fraction. Specifically, the rise in amylose content and low M_w starch content led to a greater likelihood of forming a complex with RA under high temperature and pressure during the HPH process. Therefore, the interactions, especially CH-π interaction, in HPH-Pα-RA complexes were stronger than in HPH-P-RA, leading to elevated levels of ordered structures as mentioned earlier and ultimately enhancing its *in vitro* digestibility.

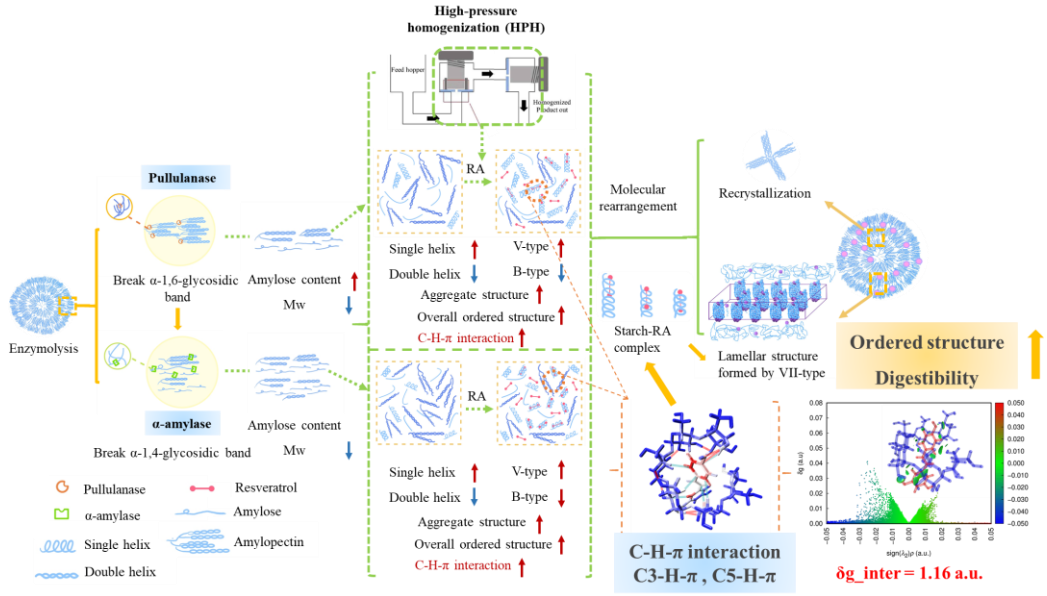

Figure 6. Mechanisms of CH-π interaction alter the structure and digestibility of starch-RA complexes via the HPH process.

4 Conclusion

This study aimed to explore the impact of RA interactions with high-amylose starch on the digestibility and ordered structural changes of this starch with varying M_w formed via the HPH process. Notably, RA, with its extensive π plane conjugation and minimal steric hindrance, facilitated weak CH-π interaction, differing from conventional hydrogen bonding in starch-RA complexes. The enzymatic treatment using pullulanase and subsequently using α-amylase effectively increased amylose content while reducing M_w, resulting in Pα samples. This led to enhanced interactions with RA, particularly through CH-π interaction. Although RA-starch inclusion complexes inhibited the formation of double helices and the B-type crystalline structure, they significantly improved single helix formation, the V-type crystalline structure, and the aggregate density. This complexation ultimately increased the overall ordered structures, resulting in a remarkable RS content of 57.37% in the HPH-Pα2-RA complexes. These findings provide insights into the interactions between starch and RA and the design of starch-RA complexes with higher RS content using HPH processing, promising applications in the development of functional food products with enhanced nutritional benefits.

ABBREVIATIONS

G50, High-amylose corn starch; RA, Resveratrol; HPH, High-pressure homogenization; RC, Relative crystallinity; RDS, Rapidly digestible starch; SDS, Slowly digestible starch; RS, Resistant starch.

CRediT authorship contribution statement

Zhipeng Qiu: Conceptualization, Methodology, Resources, Supervision, Project

administration, Writing - Review & Editing; **Rui Li**: Methodology, Validation, Formal analysis, Investigation, Data Curation, Writing - Original Draft, Visualization; **Jin Chen**: Formal analysis, Investigation, Data Curation, Writing - Original Draft; **Ling Chen**: Methodology, Resources, Writing - Review & Editing, Visualization, Supervision, Funding acquisition; **Fengwei Xie**: Methodology, Writing - Review & Editing.

Declaration of competing interest

The authors declare no competing financial interests.

Acknowledgements

This research has been financially supported by the National Natural Science Foundation of China (32172167), and the Guangdong Basic and Applied Basic Research Foundation (2022A1515110661).

References:

Amoako, D. B., & Awika, J. M. (2016). Polymeric tannins significantly alter properties and in vitro digestibility of partially gelatinized intact starch granule. *Food Chemistry, 208*, 10-17.

Asensio, J. L., Arda, A., Canada, F. J., & Jimenez-Barbero, J. (2013). Carbohydrate-Aromatic Interactions. *Accounts of Chemical Research, 46*(4), 946-954.

Barros, F., Awika, J. M., & Rooney, L. W. (2012). Interaction of Tannins and Other Sorghum Phenolic Compounds with Starch and Effects on in Vitro Starch Digestibility. *Journal of Agricultural and Food Chemistry, 60*(46), 11609-11617.

Biais, B., Le Bail, P., Robert, P., Pontoire, B., & Buleon, A. (2006). Structural and stoichiometric studies of complexes between aroma compounds and amylose. Polymorphic transitions and quantification in amorphous and crystalline areas. *Carbohydrate Polymers, 66*(3), 306-315.

Cao, W. H., Zheng, B., Zeng, X. X., & Chen, L. (2024). Stilbene, as phyto-oestrogens, can construct resistant starch through noncovalent interactions with starch: A structural correlation study. *Food Hydrocolloids, 148*, 109438.

Chao, C., Yu, J. L., Wang, S., Copeland, L., & Wang, S. J. (2018). Mechanisms Underlying the Formation of Complexes between Maize Starch and Lipids. *Journal of Agricultural and Food Chemistry, 66*(1), 272-278.

Chen, S. F., Zong, J. H., Jiang, L. J., Ma, C. Y., Li, H. J., & Zhang, D. L. (2020). Improvement of resveratrol release performance and stability in extruded microparticle by the

alpha-amylase incorporation. *Journal of Food Engineering, 274*, 109842.

Chen, X. X., Zhang, J., Yin, N., Wele, P., Li, F., Dave, S., Lin, J. Y., Xiao, H., & Wu, X. (2022). Resveratrol in disease prevention and health promotion: A role of the gut microbiome. *Critical Reviews in Food Science and Nutrition*, 1-18.

Cui, M. M., Mi, T. T., Wu, Z. Z., Gao, W., Kang, X. M., Cui, B., & Liu, P. F. (2024). Synergistic effect of enzymatic pre-treatment and amylose-lipid complex construction on the physicochemical properties of maize starch. *Food Chemistry, 434*, 137501.

Deng, N., Deng, Z., Tang, C., Liu, C. M., Luo, S. J., Chen, T. T., & Hu, X. T. (2021). Formation, structure and properties of the starch-polyphenol inclusion complex: A review. *Trends in Food Science & Technology, 112*, 667-675.

Evans, E., van Wegen, B., Ma, Y. F., & Eglinton, J. (2003). The impact of the thermostability of alpha-amylase, beta-amylase, and limit dextrinase on potential Wort fermentability. *Journal of the American Society of Brewing Chemists, 61*(4), 210-218.

Frisch, M., Trucks, G., Schlegel, H., Scuseria, G., Robb, M., Cheeseman, J., Scalmani, G., Barone, V., Petersson, G., & Nakatsuji, H. (2016). Gaussian 16. In: Gaussian, Inc. Wallingford, CT.

Gidley, M. J., & Bociek, S. M. (1988). Carbon-13 CP/MAS NMR studies of amylose inclusion complexes, cyclodextrins, and the amorphous phase of starch granules: Relationships between glycosidic linkage conformation and solid-state carbon-13 chemical shifts. *Journal of the American Chemical Society, 110*(12), 3820-3829.

Giuberti, G., Rocchetti, G., & Lucini, L. (2020). Interactions between phenolic compounds, amylolytic enzymes and starch: an updated overview. *Current Opinion in Food Science, 31*, 102-113.

Grimme, S., Antony, J., Ehrlich, S., & Krieg, H. (2010). A consistent and accurate ab initio parametrization of density functional dispersion correction (DFT-D) for the 94 elements H-Pu. *Journal of Chemical Physics, 132*(15), 154104.

Guo, L., Cui, B., Gui, Y. F., Wei, X. Y., Yang, N., Zou, F. X., Lu, L., Liu, P. F., & Fang, Y. S. (2022). Comparison of structural and functional properties of maize starch produced with commercial or endogenous enzymes. *International Journal of Biological Macromolecules, 209*, 2213-2225.

Gutierrez, T. J., & Bello-Perez, L. A. (2022). Self-assembled and assembled starch V-type complexes for the development of functional foodstuffs: A review. *Food Hydrocolloids, 125*, 107453.

Hou, C. D., Zhao, X. H., Tian, M. Q., Zhou, Y. L., Yang, R. Q., Gu, Z. X., & Wang, P. (2020). Impact of water extractable arabinoxylan with different molecular weight on the gelatinization and retrogradation behavior of wheat starch. *Food Chemistry, 318*, 126477.

Iiyama, T., Ruike, M., & Kaneko, K. (2000). Structural mechanism of water adsorption in hydrophobic micropores from in situ small angle X-ray scattering. *Chemical Physics Letters, 331*(5-6), 359-364.

Jimenez-Moreno, E., Jimenez-Oses, G., Gomez, A. M., Santana, A. G., Corzana, F., Bastida, A., Jimenez-Barberodef, J., & Asensio, J. L. (2015). A thorough experimental study of CH/pi interactions in water: quantitative structure-stability relationships for carbohydrate/aromatic complexes. *Chemical Science, 6*(11), 6076-6085.

Kong, L. Y., Lee, C., Kim, S. H., & Ziegler, G. R. (2014). Characterization of Starch Polymorphic Structures Using Vibrational Sum Frequency Generation Spectroscopy. *Journal of Physical Chemistry B, 118*(7), 1775-1783.

Li, M., Ndiaye, C., Corbin, S., Foegeding, E. A., & Ferruzzi, M. G. (2020). Starch-phenolic complexes are built on physical CH-pi interactions and can persist after hydrothermal treatments altering hydrodynamic radius and digestibility of model starch-based foods. *Food Chemistry, 308*, 125577.

Lin, Y. C., Hu, S. C. S., Huang, P. H., Lin, T. C., & Yen, F. L. (2020). Electrospun Resveratrol-Loaded Polyvinylpyrrolidone/Cyclodextrin Nanofibers and Their Biomedical Applications. *Pharmaceutics, 12*(6), 552.

Liu, P. F., Fang, Y. S., Zhang, X. L., Zou, F. X., Gao, W., Zhao, H. B., Yuan, C., & Cui, B. (2020). Effects of multienzyme treatment on the physicochemical properties of maize starch-lauric acid complex. *Food Hydrocolloids, 107*, 105941.

Liu, P. F., Kang, X. M., Cui, B., Gao, W., Wu, Z. Z., & Yu, B. (2019). Effects of amylose content and enzymatic debranching on the properties of maize starch-glycerol monolaurate complexes. *Carbohydrate Polymers, 222*, 115000.

Liu, Y. F., Chen, L., Xu, H. S., Liang, Y., & Zheng, B. (2019). Understanding the digestibility of rice starch-gallic acid complexes formed by high pressure homogenization. *International Journal of Biological Macromolecules, 134*, 856-863.

Liu, Z. P., Chen, L., & Zheng, B. (2022). Control of starch-lipid interactions on starch digestibility during hot-extrusion 3D printing for starchy foods. *Food & Function, 13*(9), 5317-5326.

Lopez-Rubio, A., Flanagan, B. M., Gilbert, E. P., & Gidley, M. J. (2008). A novel approach for calculating starch crystallinity and its correlation with double helix content: A combined XRD and NMR study. *Biopolymers, 89*(9), 761-768.

Lu, T., & Chen, F. W. (2012). Multiwfn: A multifunctional wavefunction analyzer. *Journal of Computational Chemistry, 33*(5), 580-592.

Lu, T., & Chen, Q. X. (2022). Independent gradient model based on Hirshfeld partition: A new method for visual study of interactions in chemical systems. *Journal of Computational Chemistry, 43*(8), 539-555.

Qiu, Z., Chen, L., Rao, C., & Zheng, B. (2023). Starch-Guar gum-Ferulic acid Molecular Interactions Alter the Ordered Structure and Ultimate Retrogradation Properties and In Vitro Digestibility of Chestnut Starch under Extrusion Treatment. *Food Chemistry, 416*, 135803.

Qiu, Z., Zeng, X., Xu, J., Zheng, B., & Chen, L. (2023). Regioselective C6-OH oxidation of starch by laccase-TEMPO-system: A multi-scale structure evolution and water absorption properties study. *Industrial Crops and Products, 193*, 116148.

Qiu, Z. P., Zheng, B., Xu, J. C., Chen, J., & Chen, L. (2022). 3D-printing of oxidized starch-based hydrogels with superior hydration properties. *Carbohydrate Polymers, 292*, 119686.

Raju, R. K., Ramraj, A., Hillier, I. H., Vincent, M. A., & Burton, N. A. (2009). Carbohydrate-aromatic pi interactions: a test of density functionals and the DFT-D method. *Physical Chemistry Chemical Physics, 11*(18), 3411-3416.

Ribeiro, J. P., Bacchi, S., Dell'Anna, G., Morando, M., Cañada, F. J., Cozzi, F., & Jiménez-Barbero, J. (2008). A Combined NMR, Computational, and HPLC Study of the Inclusion of Aromatic and Fluoroaromatic Compounds in Cyclodextrins as a Model for Studying Carbohydrate–Aromatic Interactions. *European Journal of Organic Chemistry, 35*, 5891-5898.

Tan, X., Li, X., Chen, L., Xie, F., Li, L., & Huang, J. (2017). Effect of heat-moisture treatment on multi-scale structures and physicochemical properties of breadfruit starch. *Carbohydrate Polymers, 161*, 286-294.

Wang, B., Li, D., Wang, L. J., Liu, Y. H., & Adhikari, B. (2012). Effect of high-pressure homogenization on microstructure and rheological properties of alkali-treated high-amylose maize starch. *Journal of Food Engineering, 113*(1), 61-68.

Wang, C. H., Zhu, Z. J., Mei, L. P., Xia, Y. Y., Chen, X., Mustafa, S., & Du, X. F. (2023). The structural properties and resistant digestibility of maize starch-glyceride monostearate complexes. *International Journal of Biological Macromolecules, 249*, 126141.

Wang, S. J., Chao, C., Cai, J. J., Niu, B., Copeland, L., & Wang, S. (2020). Starch-lipid and starch-lipid-protein complexes: A comprehensive review. *Comprehensive Reviews in Food*

Science and Food Safety, 19(3), 1056-1079.

Wang, S. J., Wang, S. K., Guo, P., Liu, L., & Wang, S. (2017). Multiscale Structural Changes of Wheat and Yam Starches during Cooking and Their Effect on in Vitro Enzymatic Digestibility. *Journal of Agricultural and Food Chemistry, 65*(1), 156-166.

Wang, X. Y., Nie, Y., & Xu, Y. (2019). Industrially produced pullulanases with thermostability: Discovery, engineering, and heterologous expression. *Bioresource Technology, 278*, 360-371.

Wu, M., Luo, Q. Y., Nie, R. X., Yang, X. P., Tang, Z. Z., & Chen, H. (2021). Potential implications of polyphenols on aging considering oxidative stress, inflammation, autophagy, and gut microbiota. *Critical Reviews in Food Science and Nutrition, 61*(13), 2175-2193.

Yang, D. Y., Guo, Q. Y., Li, R., Chen, L., & Zheng, B. (2024). Amylose content controls the V-type structural formation and digestibility of maize starch-resveratrol complexes and their effect on human gut microbiota. *Carbohydrate Polymers, 327*, 121702.

Zeng, X. X., Zheng, B., Li, T. J., & Chen, L. (2022). How to synchronously slow down starch digestion and retrogradation: A structural analysis study. *International Journal of Biological Macromolecules, 212*, 43-53.

Zhang, J., & Lu, T. (2021). Efficient evaluation of electrostatic potential with computerized optimized code. *Physical Chemistry Chemical Physics, 23*(36), 20323-20328.

Zhang, L. L., Li, X. X., Janaswamy, S., Chen, L., & Chi, C. D. (2020). Further insights into the evolution of starch assembly during retrogradation using SAXS. *International Journal of Biological Macromolecules, 154*, 521-527.

Zhang, Z. J., Zheng, B., Du, A. L., Chen, J., & Chen, L. (2023). Insight into the retardation of retrogradation of chestnut starch by heat-moisture treatment with flavonoids. *Food Chemistry, 404*, 134587.

Zhao, B., Wang, B., Zheng, B., Chen, L., & Guo, Z. (2019). Effects and mechanism of high-pressure homogenization on the characterization and digestion behavior of lotus seed starch–green tea polyphenol complexes. *Journal of Functional Foods, 57*, 173-181.

Zheng, B., Liu, Z. P., Chen, L., Qiu, Z. P., & Li, T. J. (2022). Effect of starch-catechin interaction on regulation of starch digestibility during hot-extrusion 3D printing: Structural analysis and simulation study. *Food Chemistry, 393*, 133394.

Zheng, B., Wang, T. T., Wang, H. W., Chen, L., & Zhou, Z. K. (2020). Studies on nutritional intervention of rice starch- oleic acid complex (resistant starch type V) in rats fed by high-fat diet. *Carbohydrate Polymers, 246*, 116637.

Zou, W., Yu, L., Liu, X. X., Chen, L., Zhang, X. Q., Qiao, D. L., & Zhang, R. Z. (2012). Effects of amylose/amylopectin ratio on starch-based superabsorbent polymers. *Carbohydrate Polymers, 87*(2), 1583-1588.

Favored CH-π interaction between enzymatically modified high amylose starch and resveratrol improves digestion resistance

Zhipeng Qiu[a], RuiLi[a], Jin Chen[a*], Ling Chen[a**], Fengwei Xie[b]

[a]School of Food Science and Engineering, Guangdong Province Key Laboratory for Green Processing of Natural Products and Product Safety, Engineering Research Center of Starch and Vegetable Protein Processing Ministry of Education, South China University of Technology, Guangzhou 510640, China

[b]School of Engineering, Newcastle University, Newcastle Upon Tyne, NE1 7RU, United Kingdom

* Corresponding author: bravojinchen@scut.edu.cn (Jin Chen);

** Corresponding author: felchen@scut.edu.cn; (Ling Chen)

Materials and methods

Molecular weight

For each sample, 5 mg of starch was dispersed in 5 mL of dimethyl sulfoxide (DMSO) containing LiBr (50 mM) and then heated at 110 °C for 1 h. Then, the completely dissolved sample solutions were filtered using a 5 μm membrane filter (Millipore Co., USA) and transferred to sample bottles. The GPC system consisted of a pump (1515, Waters, Milford, MA, USA), an auto-injector with a 0.1 mL loop (717, Waters), and three columns (Sytyragel HMW7 GPC column, Sytyragel HMW6E GPC column, and Sytyragel HMW2 GPC column, respectively, 7.8 × 300 mm, Waters) (J. Chen, Li, Chen, & Xie, 2018).

In vitro digestibility

In a 100 mL conical flask containing 20 mL of sodium acetate buffer, 1 g of starch (dry basis) was added. Following that, a 5 mL mixture of porcine pancreatic amylase and starch glucosidase was introduced into the flask. The flask was then placed into a water bath oscillator with a constant temperature set at 37 °C and 190 rpm, and allowed to react for 20 min and 120 min. After the reaction, 0.5 mL of the resulting solution was transferred to a 50 mL centrifuge tube containing 20 mL of 70% ethanol to inactivate the enzyme. The glucose concentration in the hydrolysate was measured using the GOPOD method. The contents of rapidly digestible starch (RDS), slowly digestible starch (SDS), and resistant starch (RS) were determined.

RA release assay

RA release assay was measured by the Folin-Ciocalteu method according to the previous study (Stojanovic et al., 2012). Briefly, 1 g HPH-RA samples (on a starch dry

basis) were hydrolyzed at 37 °C using a blend of porcine pancreatin and amyloglucosidase according to *In vitro* digestibility test. After 5, 10, 20, 60 and 120 min, 0.5 mL of the solution was transferred to a 50 mL centrifuge tube containing 20 mL of 70% ethanol to inactivate the enzyme. 0.5 mL supernatant was thoroughly mixed with 1 mL of Folin-Ciocalteu reagent (10%, v/v). Then, 2 mL of 15% (w/v) sodium carbonate was added to the mixture and the sample was allowed to stand for 60 min at room temperature. Finally, the absorbance of the samples was tested at 760 nm and the RA release were calculated according to the standard curve.

Helical structures

The helical structures of the samples were analyzed using a solid-state carbon-13 nuclear magnetic resonance (^{13}C NMR) spectrometer, specifically a Bruker AVANCE III HD 400 model (Bruker, Germany). To obtain a clear signal, a sample weighing 200 mg was placed on the 4 mm MAS fixed probe, as described in previous studies, and the analysis was performed with 1600 scans (He, Zheng, Wang, Li, & Chen, 2020; Zheng, Wang, Wang, Chen, & Zhou, 2020).

Crystalline structures

The crystalline structures of the samples were determined using an X-ray diffractometer (PANalytical Co., Almelo, Netherlands). The scan range covered 5 to 45°, with a step width of 0.033° and a speed of 10°/min, while the voltage and amperage were maintained at 40 kV and 40 mA, respectively. The MDI Jade software (Version 6.0) was employed to compute the crystallinity type and relative crystallinity (RC), as previously reported (Zeng, Zheng, Li, & Chen, 2022; Zheng, et al., 2020).

$$\text{Total area} = \text{Peak area of B} - \text{type and V} - \text{type crystalline} + \text{Peak area of amorphous portion} \quad (1)$$

$$\mathrm{B-type\ (\%)} = \frac{\text{Peak area of B-type crystalline}}{\text{Total area}} \times 100 \quad (2)$$

$$\mathrm{V-type\ (\%)} = \frac{\text{Peak area of V-type crystalline}}{\text{Total area}} \times 100 \quad (3)$$

$$\mathrm{RC(\%)} = \mathrm{B-type\ (\%) + V-type\ (\%)} \quad (4)$$

Aggregated structures

To obtain detailed information on the fractal dimension and network structure of the starch complex gel, monochrome Cu-K with a wavelength of 0.1542 nm was used to analyze the gel samples at a test temperature of 25 °C. The test tube pressure and tube flow were set as 40 kV and 50 mA, respectively. SAXSquant2D and SAXSquant2D software were used to normalize and subtract the background of the test data of the samples (Iiyama, Ruike, & Kaneko, 2000; Qiu, Zheng, Xu, Chen, & Chen, 2022).

$$\mathrm{I(q)}=\mathrm{I}_{OZ}(0)/(1+\xi^2\mathrm{q}^2) \quad (5)$$

$$\mathrm{I(q)}=\mathrm{I}_{OZ}(0)/(1+\Sigma^2\mathrm{q}^2) + Aq^{-\delta} \quad (6)$$

Where q (nm^{-1}) is the scattering vector of the sample, $I(q)$ (a.u.) is the scattering intensity, and $I_{OZ}(0)$ (a.u.) is the scattering intensity at a zero-degree angle, ξ (nm) is the relevant length, Σ is the characteristic length (nm) characterizing the degree of heterogeneity of the system.

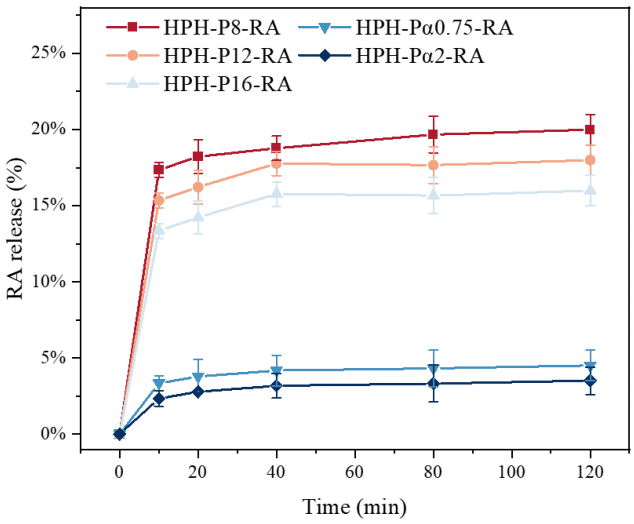

Figure S1 RA release of HPH-RA complexes during digestion.

Table S1. Molecular weight and distribution of the starch samples.

Samples	amylose content (%)	M_w (× 10^5 g/mol)	<2×10^{4a} (%)	2-5×10^{4a} (%)	5×10^{4a}-1×10^{5a} (%)	1-5×10^{5a} (%)	5×10^{5a}-1×10^{6a} (%)	>1×10^{6a} (%)
G50	50.03±0.11^{e}	25.92	0	0	0	0	47.15	52.82
P-8h	63.92±0.84^{d}	9.359	0.11	0.24	1.15	11.14	52.25	35.11
HPH-P8	66.33±0.56^{c}	5.721	0.24	1.45	5.67	33.55	30.26	28.83
HPH-P8-RA	67.10±0.34^{c}	5.524	0.22	2.47	6.32	34.22	30.21	26.56
P-12h	78.42±0.45^{b}	8.325	0.72	1.20	8.65	15.12	50.06	24.25
HPH-P12	80.34±0.45^{b}	5.543	0.98	3.23	14.06	16.32	44.76	16.65
HPH-P12-RA	80.88±0.55^{b}	5.041	0.88	3.65	16.04	19.97	44.11	15.35
P-16h	84.46±0.61^{a}	5.906	1.94	4.31	16.50	22.14	41.25	13.86
HPH-P16	85.32±0.44^{a}	5.291	2.78	7.34	18.55	24.69	36.32	10.32
HPH-P16-RA	85.11±0.27^{a}	5.046	2.96	7.01	19.45	23.58	37.11	9.89
P-α-0.75h	77.56±0.74^{b}	2.148	3.12	15.02	18.72	45.48	16.23	1.43
HPH-Pα0.75	77.49±0.71^{b}	1.901	4.54	18.34	23.99	40.67	12.46	0
HPH-Pα0.75-RA	77.92±0.49^{b}	1.892	5.31	17.59	23.68	41.74	11.68	0
P-α-2h	76.42±0.69^{b}	0.697	16.70	36.16	31.44	15.00	0.70	0
HPH-Pα2	76.88±0.75^{b}	0.693	18.33	43.48	25.87	12.32	0	0
HPH-Pα2-RA	76.12±0.56 ^{b}	0.688	18.67	42.99	24.32	14.02	0	0

Values are presented as means ± SD; The different letters were significantly different ($p < 0.05$).

Table S2. Digestibility of the simple mixture of HPH samples with corresponding released RA

Samples	RDS (%)	SDS (%)	RS (%)
M-HPH-P8-RA	59.43±0.43^{a}	14.45±0.39^{a}	26.12±0.84^{e}
M-HPH-P12-RA	53.47±0.33^{b}	11.67±0.79^{c}	32.86±1.42^{d}
M-HPH-P16-RA	52.33±0.24^{b}	12.98±0.11^{b}	33.69±0.13^{c}
M-HPH-Pα0.75-RA	48.87±0.52^{c}	14.21±0.33^{a}	36.92±0.54^{b}
M-HPH-Pα2-RA	48.11±0.66^{c}	12.82±0.73^{b}	39.07±0.45^{a}

Values are presented as means ± SD; The different letters were significantly different ($p < 0.05$).

Reference

He, H., Zheng, B., Wang, H. W., Li, X. X., & Chen, L. (2020). Insights into the multi-scale structure and in vitro digestibility changes of rice starch-oleic acid/linoleic acid complex induced by heat-moisture treatment. *Food Research International, 137*, 109612.

Iiyama, T., Ruike, M., & Kaneko, K. (2000). Structural mechanism of water adsorption in hydrophobic micropores from in situ small angle X-ray scattering. *Chemical Physics Letters, 331*(5-6), 359-364.

Qiu, Z. P., Zheng, B., Xu, J. C., Chen, J., & Chen, L. (2022). 3D-printing of oxidized starch-based hydrogels with superior hydration properties. *Carbohydrate Polymers, 292*, 119686.

Zeng, X. X., Zheng, B., Li, T. J., & Chen, L. (2022). How to synchronously slow down starch digestion and retrogradation: A structural analysis study. *International Journal of Biological Macromolecules, 212*, 43-53.

Zheng, B., Wang, T. T., Wang, H. W., Chen, L., & Zhou, Z. K. (2020). Studies on nutritional intervention of rice starch- oleic acid complex (resistant starch type V) in rats fed by high-fat diet. *Carbohydrate Polymers, 246*, 116637.